

Modeling, Simulation and Characterization of Atomic Force Microscopy Measurements for Ionic Transport and Impedance in PEM Fuel Cells

Investigators

Peter M. Pinsky, Professor, Mechanical Engineering; David M. Barnett, Professor, Materials Science and Engineering and Mechanical Engineering; Yongxing Shen, Graduate Researcher

Introduction

Solid polymer fuel cells promise to be an efficient power source for mobile and stationary applications with the potential for a greatly reduced environmental impact. However, the ionic diffusion behavior under current load conditions in the ion-selective membranes of proton exchange membrane fuel cells (PEMFCs) is not completely understood. Further understanding of ion behavior at the Nernst diffusion layer of the membrane surface could enable the development of new classes of solid polymer fuel cell membranes with increased mass transport.

In this project we are examining and characterizing the properties of solid polymer membranes through analytical and numerical modeling of ion transport, impedance, diffusion and atomic force microscopy imaging. To address the challenges of enabling new solid polymer fuel cell membranes, the project has four primary objectives:

1. *Atomic force microscope imaging.* Nanoscale AFM surface imaging of dielectric or polarizable fuel cell materials involves complex AFM tip interactions with unknown surface and space charges resulting in electrostatic and van der Waals forces. Nonlinear modeling will be employed to solve the inverse problem of finding the charge distributions from AFM images with the goal of elucidating the mechanisms of charge motion in fuel cell and biological media relevant for environmental cleanup.
2. *Simulation of impedance measurements.* Modeling and simulation of AFM impedance measurements in fuel cells to shed light on the effects of probe tip geometry, surface roughness and topography with goal of developing scaling laws for fuel cell performance.
3. *Modeling of ionic transport in PEMFC's.* Analytical and numerical modeling of ionic diffusion in fuel cells taking into account electrochemical kinetics, current distribution, hydrodynamics and multi-component transport with goal of elucidating mass transport characteristics.
4. *Particle diffusion modeling.* In order to further understand mechanisms of ion and solvent transport in hydrated PEMFC membranes, modeling that accounts for local molecular information will be employed.

Our initial efforts in starting the project have been directed to the first objective and our preliminary findings are reported below.

Atomic Force Microscopy (AFM) has been and continues to be the prominent method for imaging and characterizing the surfaces of fuel cell materials. Such imaging is absolutely essential for understanding why certain designs, selections, and processing of fuel cell membrane materials prove to be successful or unsuccessful choices. In this sense the AFM is currently as crucial to fuel cell technology development as is imaging by electromagnetic and other radiation in modern medicine and health care.

In essence the AFM is a cantilever beam with a charged tip (of somewhat variable geometry) which can scan a sample (the fuel cell material of interest) either separated from it or intermittently in contact with it. Electronics and control circuits may be used to maintain a fixed tip to sample distance or, say, a constant capacitive force. If the tip-sample interaction can be appropriately modeled, sample surface charge distribution and local surface impedance can be predicted for comparison with experimental measurements and observations. Local impedance measurements are now commonly obtained for purposes of assessing fuel cell membrane quality, but usually using equivalent circuit lump parameter models rather than sound microscopic modeling. It seems clear that the ability to rationally select and process better fuel cell materials will require a deeper understanding of microscopic mechanistic modeling that currently exists.

Background

The AFM tip-sample interaction is dominated by electrostatic force when they are distantly separated (while Van der Waals forces are predominant in the short range regime). The electrostatic forces depend on the material characteristic of interest (surface topography and charge distribution), the tip properties (conductive/dielectric, tip shape) and the force detection scheme. The physical picture is schematically displayed in Fig. 1. One goal of our research is to advance our ability to perform quantitative imaging by modeling the relevant tip-sample interactions.

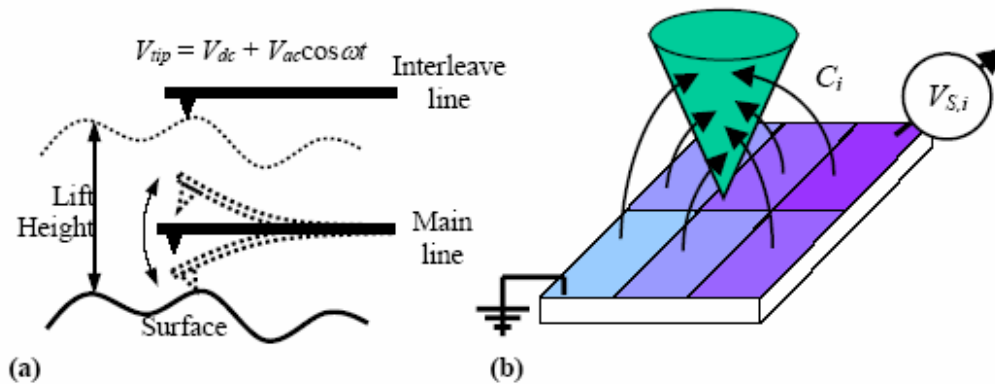


Figure 1: Set-up for scanning capacitance microscope (a) and illustration of how a potential distribution on a sample surface contributes to the tip capacitance (from [7]).

For a conductive tip at a constant potential, the electrostatic force between the tip and the sample is the capacitive force. A number of approximate models have been proposed

to quantify this capacitive force between the biased tip and the grounded surface. These models can be categorized into two families:

Family 1: Tip of simple geometric shape

This family of models describes the tip as a simple geometric object such as a plate capacitor, a sphere [1], a hyperboloid [2], a cone [3], or a cone with a spherical apex [4]. Because of the geometric simplification of the tip shape, these analytical approaches are not capable of capturing the details of the tip, and not generalizable to more complex tip shapes.

Family 2: Tip represented by an equipotential

Another family of models represents the charge of the tip as a fictitious distribution of charge along the AFM tip axis and the tip surface as one of the equipotentials due to the presence of such charge and the sample surface. Examples are the single point charge model, the model of a series of point charges [5] and the uniformly charged line model [6]. In these models, image charge methods have been employed to ease the calculation of the equipotentials. These models imply that the actual tip shape varies with the separation from the sample, which is not realistic. Moreover, the actual tip shape would usually not be coincident with an equipotential surface resulting from a simple charge distribution.

Results

In order to overcome the limitations of the existing models and take into account the true geometry of the tip, we are developing two approaches: an analytical method based on a Green's function method and a numerical method based on finite element analysis.

1) Construction of the geometry

We have firstly examined when the sample surface is flat, grounded and infinitely extended in two dimensions, while the tip is infinite in the longitudinal direction. Consider a semicircular domain in 2D or hemispherical domain in 3D of radius R and centered at O , where O is the projection of the tip on the sample surface, as in Figure 2. Since we will eventually let R tend to infinity after solving the problem, the choice of the actual position of O is immaterial unless there is a symmetry point on the sample surface, which would be a reasonable selection of O . Let V_0 denote the domain bounded by the semicircle (hemisphere) and $V = V_0 - V_{tip}$ (see Figure 3), where V_{tip} is the spatial domain of the tip. In the domain V , which is a vacuum, Laplace's equation holds because there is no net charge within V .

$$\nabla^2 \phi = 0 \tag{1}$$

where ϕ is the electrostatic potential. The boundary conditions of (1) are:

$$\phi = 0 \text{ on the flat surface } S_{flat}; \tag{2a}$$

$$\phi = \phi_0 \text{ on the tip surface } S_{tip}; \tag{2b}$$

$$\frac{\partial \phi}{\partial \mathbf{n}} = 0 \text{ on } S_R, \text{ the rest of the boundary of } V. \tag{2c}$$

where \mathbf{n} is the outer normal.

Condition (2c) would be exactly the case when $R \gg z$, where z is the tip sample separation. To simplify the calculation, we would first solve (1) using (2c) with finite R

and then let R approach infinity. Eq. (1), together with (2a)—(2c), can be solved using the finite element method. On the other hand, we have also developed a Green's function method for the capacitance which produces an exact analytic derivation suitable for constructing a variational technique amenable to both analytical and numerical studies.

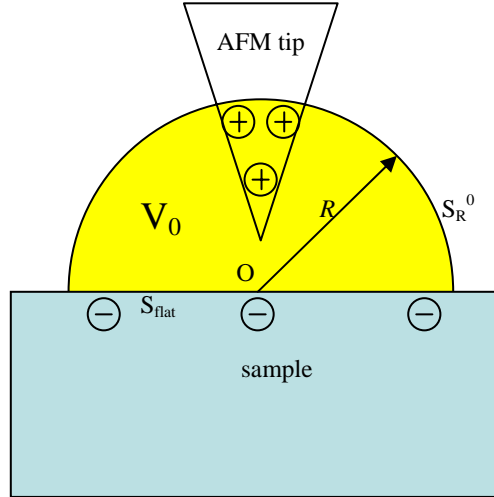


Figure 2: Construction of the very large semicircle (hemisphere).

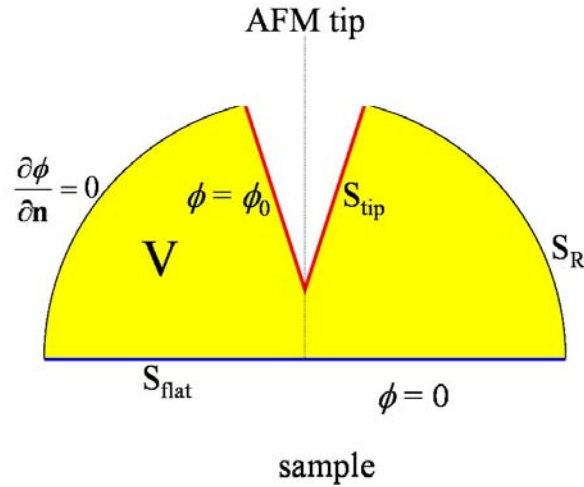


Figure 3: Boundary conditions for domain V .

2) *Derivation of the boundary integral equation for the surface charge density of the tip*
Construct the Green's function $G(\mathbf{r}, \mathbf{r}')$ such that,

$$\nabla_{\mathbf{r}}^2 G = -\frac{\delta(\mathbf{r} - \mathbf{r}')}{\epsilon_0}; \quad (3a)$$

$$G = 0 \text{ on } S_{\text{flat}}; \quad (3b)$$

$$\frac{\partial G}{\partial \mathbf{n}} = 0 \text{ on } S_R^0; \quad (3c)$$

where ϵ_0 is the dielectric constant for vacuum.

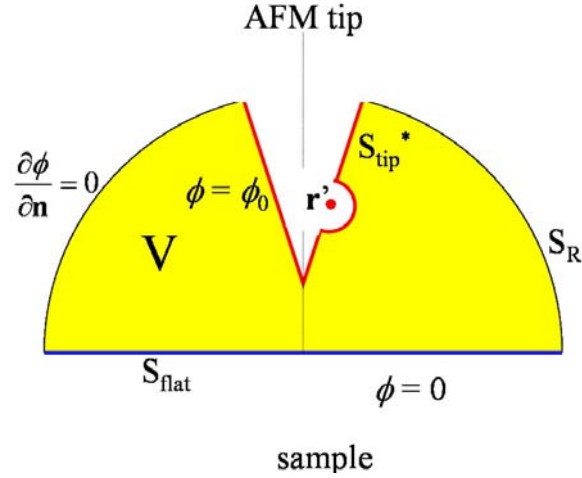


Figure 4: Geometric construction of domain V^* , which is V less a semicircle (or hemisphere).

If the source point \mathbf{r}' lies in V , we can write, using Green's theorem,

$$\begin{aligned} & \iiint_V [G(\mathbf{r}, \mathbf{r}') \nabla^2 \phi(\mathbf{r}) - \phi(\mathbf{r}) \nabla_{\mathbf{r}'}^2 G(\mathbf{r}, \mathbf{r}')] dV(\mathbf{r}) \\ &= \iint_{S_{\text{flat}} + S_{\text{tip}} + S_R} \left[G(\mathbf{r}, \mathbf{r}') \frac{\partial \phi(\mathbf{r})}{\partial \mathbf{n}(\mathbf{r})} - \phi(\mathbf{r}) \frac{\partial G(\mathbf{r}, \mathbf{r}')}{\partial \mathbf{n}(\mathbf{r})} \right] dS(\mathbf{r}) \end{aligned} \quad (4)$$

Using (1) and (3a) on the left hand side and (2a), (2b), (2c), (3b) and (3c) on the right hand side, (4) can be reduced to

$$\phi(\mathbf{r}') = \varepsilon_0 \iint_{S_{\text{tip}}} \left[G(\mathbf{r}, \mathbf{r}') \frac{\partial \phi(\mathbf{r})}{\partial \mathbf{n}(\mathbf{r})} - \phi(\mathbf{r}) \frac{\partial G(\mathbf{r}, \mathbf{r}')}{\partial \mathbf{n}(\mathbf{r})} \right] dS(\mathbf{r}); \quad \mathbf{r}' \text{ in } V. \quad (5)$$

Now we consider when \mathbf{r}' is on S_{tip} . As in classical boundary integral equation methods, let \mathbf{r}' lie on S_{tip} and apply Green's theorem to an "indented contour (or indented surface)" as shown in Figure 4, then we have

$$\begin{aligned} & \iiint_{V^*} [G(\mathbf{r}, \mathbf{r}') \nabla^2 \phi(\mathbf{r}) - \phi(\mathbf{r}) \nabla_{\mathbf{r}'}^2 G(\mathbf{r}, \mathbf{r}')] dV(\mathbf{r}) \\ &= \iint_{S_{\text{flat}} + S_{\text{tip}}^* + S_R} \left[G(\mathbf{r}, \mathbf{r}') \frac{\partial \phi(\mathbf{r})}{\partial \mathbf{n}(\mathbf{r})} - \phi(\mathbf{r}) \frac{\partial G(\mathbf{r}, \mathbf{r}')}{\partial \mathbf{n}(\mathbf{r})} \right] dS(\mathbf{r}) \end{aligned} \quad (6)$$

Since \mathbf{r}' is outside V^* , in V^* we have $\nabla_{\mathbf{r}'}^2 G = 0$ and of course $\nabla^2 \phi = 0$. Thus

$$\iint_{S_{\text{flat}} + S_{\text{tip}}^* + S_R} \left[G(\mathbf{r}, \mathbf{r}') \frac{\partial \phi(\mathbf{r})}{\partial \mathbf{n}(\mathbf{r})} - \phi(\mathbf{r}) \frac{\partial G(\mathbf{r}, \mathbf{r}')}{\partial \mathbf{n}(\mathbf{r})} \right] dS(\mathbf{r}) = 0. \quad (7)$$

Applying (2a), (2c), (3b), and (3c) to (7) yields

$$\iint_{S_{\text{tip}}^*} \left[G(\mathbf{r}, \mathbf{r}') \frac{\partial \phi(\mathbf{r})}{\partial \mathbf{n}(\mathbf{r})} - \phi(\mathbf{r}) \frac{\partial G(\mathbf{r}, \mathbf{r}')}{\partial \mathbf{n}(\mathbf{r})} \right] dS(\mathbf{r}) = 0. \quad (8)$$

Now on the “non-indented” part of S_{tip}^* , $\phi = \phi_0$. On the “indentation”, $\phi(\mathbf{r}) = \phi(\mathbf{r}') +$ terms of order ε . It is simple to show that the terms of order ε do not contribute as ε tends to zero, so that we may take $\phi(\mathbf{r}) = \phi_0$ and (8) reduces to

$$\iint_{S_{\text{tip}}^*} G(\mathbf{r}, \mathbf{r}') \frac{\partial \phi(\mathbf{r})}{\partial \mathbf{n}(\mathbf{r})} dS(\mathbf{r}) = \phi_0 \iint_{S_{\text{tip}}^*} \frac{\partial G(\mathbf{r}, \mathbf{r}')}{\partial \mathbf{n}(\mathbf{r})} dS(\mathbf{r}); \quad \mathbf{r}' \text{ on } S_{\text{tip}}^*. \quad (9)$$

To simplify the right hand side of (9), we apply Gauss’s theorem to $G(\mathbf{r}, \mathbf{r}')$ in V_0 and V^* as follows:

(1) V_0 ; \mathbf{r}' in V_0 :

$$\iiint_{V_0} \nabla_{\mathbf{r}}^2 G(\mathbf{r}, \mathbf{r}') dV(\mathbf{r}) = \iint_{S_{\text{flat}} + S_{\text{R}}^0} \frac{\partial G(\mathbf{r}, \mathbf{r}')}{\partial \mathbf{n}(\mathbf{r})} dS(\mathbf{r}). \quad (10)$$

Applying (3a) and (3c) in (10) gives

$$-\frac{1}{\varepsilon_0} = \iint_{S_{\text{flat}}} \frac{\partial G(\mathbf{r}, \mathbf{r}')}{\partial \mathbf{n}(\mathbf{r})} dS(\mathbf{r}). \quad (11)$$

(2) V^* ; \mathbf{r}' not in V^* :

$$\iiint_{V^*} \nabla_{\mathbf{r}}^2 G(\mathbf{r}, \mathbf{r}') dV(\mathbf{r}) = \iint_{S_{\text{flat}} + S_{\text{tip}}^* + S_{\text{R}}^0} \frac{\partial G(\mathbf{r}, \mathbf{r}')}{\partial \mathbf{n}(\mathbf{r})} dS(\mathbf{r}). \quad (12)$$

Again, using (3a) and (3c) in (12), we have

$$0 = \iint_{S_{\text{flat}} + S_{\text{tip}}^*} \frac{\partial G(\mathbf{r}, \mathbf{r}')}{\partial \mathbf{n}(\mathbf{r})} dS(\mathbf{r}) = \iint_{S_{\text{flat}}} \frac{\partial G(\mathbf{r}, \mathbf{r}')}{\partial \mathbf{n}(\mathbf{r})} dS(\mathbf{r}) + \iint_{S_{\text{tip}}^*} \frac{\partial G(\mathbf{r}, \mathbf{r}')}{\partial \mathbf{n}(\mathbf{r})} dS(\mathbf{r}). \quad (13)$$

Now by employing (11) and (13) in (9) we have the reduced boundary integral equation:

$$\iint_{S_{\text{tip}}^*} G(\mathbf{r}, \mathbf{r}') \frac{\partial \phi(\mathbf{r})}{\partial \mathbf{n}(\mathbf{r})} dS(\mathbf{r}) = \frac{\phi_0}{\varepsilon_0}; \quad \mathbf{r}' \text{ on } S_{\text{tip}}^*. \quad (14)$$

Let ε tend to zero so that S_{tip}^* coincides with S_{tip} , and (14) is now

$$\iint_{S_{\text{tip}}} G(\mathbf{r}, \mathbf{r}') \frac{\partial \phi(\mathbf{r})}{\partial \mathbf{n}(\mathbf{r})} dS(\mathbf{r}) = \frac{\phi_0}{\varepsilon_0}; \mathbf{r}' \text{ on } S_{\text{tip}}. \quad (15)$$

From electrostatics, the surface charge density $\sigma(\mathbf{r})$ is given by

$$\sigma(\mathbf{r}) = \varepsilon_0 \frac{\partial \phi(\mathbf{r})}{\partial \mathbf{n}(\mathbf{r})}; \mathbf{r} \text{ on } S_{\text{tip}}. \quad (16)$$

The total charge Q on the tip is

$$Q = \iint_{S_{\text{tip}}} \sigma(\mathbf{r}) dS(\mathbf{r}). \quad (17)$$

Thus the capacitance of the system is

$$C = \frac{Q}{\phi_0 - 0} = \frac{Q}{\phi_0}. \quad (18)$$

Now (15) – (18) give the integral equation for the capacitance, which can be rewritten as:

$$C = \frac{\iint_{S_{\text{tip}}} \sigma(\mathbf{r}) dS(\mathbf{r})}{\phi_0}; \quad (19)$$

$$\iint_{S_{\text{tip}}} G(\mathbf{r}, \mathbf{r}') \sigma(\mathbf{r}) dS(\mathbf{r}) = \phi_0; \mathbf{r}' \text{ on } S_{\text{tip}}. \quad (20)$$

3) Establishment of variational principle for the capacitance

Define a functional,

$$\hat{C} = \frac{2}{\phi_0} \iint_{S_{\text{tip}}} \sigma(\mathbf{r}') dS(\mathbf{r}') - \frac{1}{\phi_0^2} \iint_{S_{\text{tip}}} \sigma(\mathbf{r}') dS(\mathbf{r}') \iint_{S_{\text{tip}}} G(\mathbf{r}, \mathbf{r}') \sigma(\mathbf{r}) dS(\mathbf{r}), \quad (21)$$

then for $\sigma(\mathbf{r}) = \sigma(\mathbf{r})^{\text{exact}}$, $\hat{C} = C$ and $\delta \hat{C} = 0$, thus C is a stationary value of \hat{C} . By

replacing the right hand side of (21) by its product with α and letting $\frac{\partial \hat{C}}{\partial \alpha}$ vanish, we

have the scale independent form for \hat{C} :

$$\hat{C} = \frac{\left[\iint_{S_{\text{tip}}} \sigma(\mathbf{r}') dS(\mathbf{r}') \right]^2}{\iiint_{S_{\text{tip}}} \iint_{S_{\text{tip}}} dS(\mathbf{r}) dS(\mathbf{r}') \sigma(\mathbf{r}') G(\mathbf{r}, \mathbf{r}') \sigma(\mathbf{r})} \quad (22)$$

which also satisfies $\hat{C} = C$ and $\delta\hat{C} = 0$ when $\sigma(\mathbf{r}) = \sigma(\mathbf{r})^{\text{exact}}$, and has the property of scale independence. In other words, (22) gives the same \hat{C} when we replace $\sigma(\mathbf{r})$ by $\alpha\sigma(\mathbf{r})$ where α is an arbitrary constant. This property allows us to try different trial functions of the tip surface charge density $\sigma(\mathbf{r})$ without scaling it to match the tip-sample bias to ϕ_0 .

Now we consider the property of the stationary value of \hat{C} which equals the true capacitance C . Suppose we impose a constraint so that the total charge Q on the tip is constant, then the true surface charge density $\sigma(\mathbf{r})$ would be the one that minimizes the energy stored in the capacitance. This energy is $W = \frac{1}{2} Q\phi_0 = \frac{Q^2}{2C}$; thus the maximum of the virtual capacitance \hat{C} would be the true capacitance C , namely $C = \hat{C}_{\text{max}}$.

Progress

1) Analytical expression of \hat{C} for uniformly charge distribution on the tip (2D)

We have derived the virtual capacitance \hat{C} using (22) for a uniformly charged tip of wedge shape (2D, corresponding to a cone in 3D, as shown in Figure 5) whose charged dimension is much less than the tip-sample separation z .

To perform the derivation, we need the expression for the Green's function $G(\mathbf{r}, \mathbf{r}')$ for the domain V_0 , which is given by the image charge method (2D):

$$G(\mathbf{r}, \mathbf{r}') = -\frac{1}{2\pi\epsilon_0} \ln \frac{|\mathbf{r} - \mathbf{r}'|}{|\mathbf{r} - \mathbf{r}_1'|} - \frac{1}{2\pi\epsilon_0} \ln \frac{|\mathbf{r} - \mathbf{r}_2'|}{|\mathbf{r} - \mathbf{r}_3'|} \quad (23)$$

where \mathbf{r}_1' is the mirror image of \mathbf{r}' with respect to the flat sample surface while

$$\mathbf{r}_2' = \frac{R^2}{|\mathbf{r}'|^2} \mathbf{r}', \quad \mathbf{r}_3' = \frac{R^2}{|\mathbf{r}'|^2} \mathbf{r}_1' \quad (24)$$

where we have assumed O to be the origin.

Simplification of (22) shows that the terms involving \mathbf{r}_2' and \mathbf{r}_3' make no contribution to the denominator as R tends to infinity, while an approximation of $|\mathbf{r} - \mathbf{r}_1'| \approx 2z$ is taken for the case of $\epsilon \ll z$.

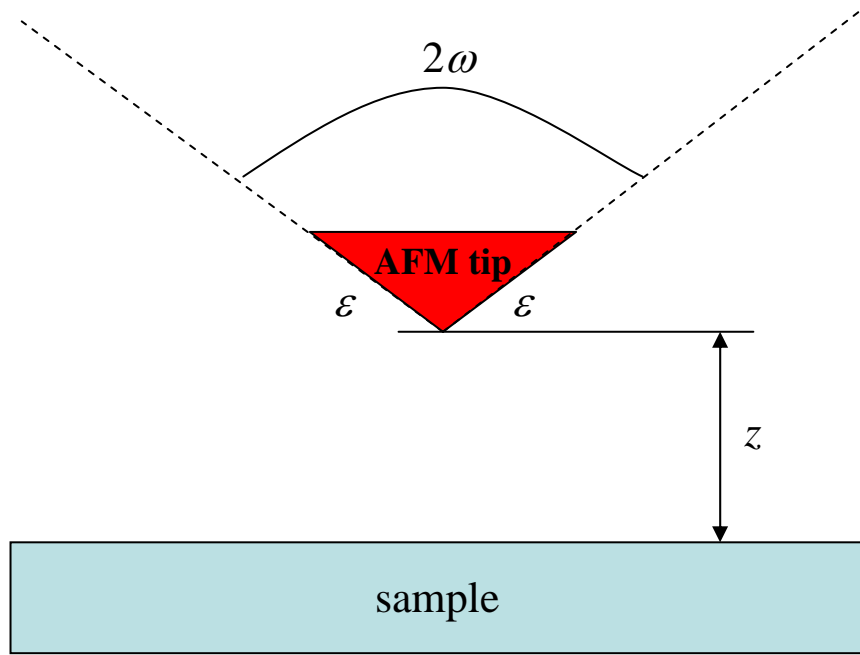


Figure 5: A wedge shape tip in 2D, or a conical tip in 3D.

The final expression for the virtual capacitance \hat{C} is

$$\hat{C} = \frac{2\pi\varepsilon_0}{\ln \frac{2e^{3/2}\beta(\omega)z}{\varepsilon}} \quad (25)$$

where ω is the semi-angle of the tip and $\beta(\omega)$ is defined as

$$\beta(\omega) = \exp\left\{-\sin \omega \left[\sin \omega \ln(2 \sin \omega) + \left(\frac{\pi}{2} - \omega\right) \cos \omega \right]\right\}. \quad (26)$$

Selected values of $\beta(\omega)$ for various ω are listed in Table I.

Table I: $\beta(\omega)$ for selected ω 's.

ω	$\beta(\omega)$
0	1.0000
$\pi/12$	0.7534
$\pi/6$	0.6354
$\pi/4$	0.5678
$\pi/3$	0.5280
$\pi/2$	0.5000

Thus \hat{C} is between $\frac{2\pi\epsilon_0}{\ln \frac{8.96z}{\epsilon}}$ and $\frac{2\pi\epsilon_0}{\ln \frac{4.48z}{\epsilon}}$, which is worth comparing with

Sneddon's result for the exact capacitance of a cylinder of radius a near a grounded plate as

$$C = \frac{2\pi\epsilon_0}{\ln \frac{2z}{a}} \quad (27)$$

where z is the shortest distance from the cylinder center to the grounded plate. The expressions (25) and (27) differ only by a factor in the argument of the logarithm, which is due to the different geometry.

2) Optimization of $\sigma(\mathbf{r})$ using a quadratic polynomial (2D)

In order to find the actual charge density on the tip and thus the capacitance, we define a generalized coordinate s along the tip contour, $s = 0$ associated with the tip vertex. By using (22), the virtual capacitance is then given by

$$\hat{C} = \frac{\left[\int_{-\epsilon}^{\epsilon} \sigma(s) ds \right]^2}{\int_{-\epsilon}^{\epsilon} ds \int_{-\epsilon}^{\epsilon} ds' \sigma(s) G(s, s') \sigma(s')} \quad (28)$$

Since (22) and thus (28) are scale independent, we can constrain those $\sigma(s)$ such that the total charge

$$Q = \int_{-\epsilon}^{\epsilon} \sigma(s) ds = \text{constant} \quad (29)$$

When $\sigma(s)$ is constant on the interval $-\epsilon \leq s \leq \epsilon$, i.e.

$$\sigma(s) = \frac{Q}{2\epsilon}; \quad -\epsilon \leq s \leq \epsilon, \quad (30)$$

we would get back to (25). Now assume $\sigma(s)$ is a linear combination of different charge density distribution, i.e.

$$\sigma(s) = \sum_{i=1}^n \alpha_i \sigma_i(s) \quad (31)$$

where each component satisfies

$$\int_{-\epsilon}^{\epsilon} \sigma_i(s) ds = Q; \quad i = 1, 2, 3 \dots n \quad (32)$$

and the coefficients satisfy

$$\sum_{i=1}^n \alpha_i = 1, \quad (33)$$

then by construction, $\sigma(s)$ automatically satisfies (29). Substituting (31) into (28) gives \hat{C} as a functions of the α_i 's with a constraint (33). Using a Lagrange multiplier on (33) to find a stationary points with respect to the α_i 's yields a system of linear equations for the α_i 's. Substituting the solution into (31) would give us the optimum $\sigma(s)$ that has the form of (31).

Consider a polynomial series with three terms, i.e.

$$\sigma_1(s) = \frac{Q}{2\varepsilon}, \sigma_2(s) = \frac{Q}{2\varepsilon} \frac{2|s|}{\varepsilon}, \sigma_3(s) = \frac{Q}{2\varepsilon} \frac{3s^2}{\varepsilon^2}. \quad (34)$$

Using the method described above, we have solved the α_i 's using numerical integration methods and obtain for $\omega \rightarrow 0$:

$$\alpha_1 = 2, \quad \alpha_2 = -3, \quad \alpha_3 = 2. \quad (35)$$

Thus we have obtained an expression $\sigma(s)$ as

$$\sigma(s) = \frac{Q}{\varepsilon} \left(1 - 3 \frac{|s|}{\varepsilon} + 3 \frac{s^2}{\varepsilon^2} \right). \quad (36)$$

which corresponds to

$$\hat{C} = \frac{2\pi\varepsilon_0}{\ln \frac{8.284z}{\varepsilon}}. \quad (37)$$

Future Plans

1) Short term plan

We plan to solve for the capacitance and thus capacitive force between the AFM tip and the sample accurately using numerical methods such as finite element analysis for different shapes of the tip and different tip-sample separations in both 2-D and 3-D.

2) Long term plan

Having accomplished our short term goal, we would extend our results to the case where the sample has inhomogeneous surface and bulk potential distribution and surface morphology. Then we would be able to understand how the AFM images are related to the transport properties of a fuel cell membrane.

Publications

None yet prepared.

References

1. Terris, B. D., Stern, J. E., Rugar, D., and Mamin, H. J., Contact electrification using force microscopy, *Phys. Rev. Lett.*, 63, 2669-2672, 1989.
2. Pan, L.-H., Sullivan, T. E., Peridier, V. J., Culter, P. H., and Miskovsky, N. M., Three-dimensional electrostatic potential, and potential-energy barrier, near a tip-base junction, *Appl. Phys. Lett.*, 65, 2151-2153, 1994
3. Yokoyama, H., Inoue, T., and Itoh, J., Nonresonant detection of electric force gradients by dynamic force microscopy, *App. Phys. Lett.*, 65, 3143-3145, 1994.
4. Hudlet, S., Jean, M. S., Guthmann, C., and Berger J., Evaluation of the capacitive force between an atomic force microscopy tip and a metallic surface, *Eur. Phys. J. B* 2, 5-10, 1998.
5. Belaidi, S., Girard, P., and Leveque, G., Electrostatic forces acting on the tip in atomic force microscopy: modelization and comparison with analytic expressions, *J. Appl. Phys.*, 81, 1023-1030, 1997.
6. Hao, H. W., Baró, A. M., and Sáenz, J. J., Electrostatic and contact forces in force microscopy, *J. Vac. Sci. Technol. B* 9, 1323-1328, 1990.
7. Kalinin, S.V. "Nanoscale electric phenomena at oxide surfaces and interfaces by scanning probe microscopy," Ph.D. dissertation, University of Pennsylvania, 2002.

Contacts

Peter M. Pinsky: pinsky@stanford.edu

David M. Barnett: barnett@stanford.edu